Journal of Alloys and Compounds 736 (2018) 152–162

Contents lists available at ScienceDirect

Journal of Alloys and Compounds

journal homepage: http://www.elsevier.com/locate/jalcom

Formation and implantation of gold nanoparticles by ArF-excimer laser irradiation of gold-coated float glass

Maximilian Heinz [a], Vasiliy V. Srabionyan [b], Leon A. Avakyan [b], Aram L. Bugaev [c, d], Anna V. Skidanenko [b], Vasiliy V. Pryadchenko [b], Jürgen Ihlemann [e], Jörg Meinertz [e], Christian Patzig [f], Manfred Dubiel [a], Lusegen A. Bugaev [b, *]

[a] Martin Luther University Halle-Wittenberg, Institute of Physics, Von-Danckelmann-Platz 3, D-06120, Halle (Saale), Germany
[b] Southern Federal University, Department of Physics, Zorge Str. 5, RU-344090, Rostov-on-Don, Russia
[c] Southern Federal University, The Smart Materials Research Center, Sladkova 178/24, RU-344090, Rostov-on-Don, Russia
[d] University of Turin, Department of Chemistry, Via P. Giuria 7, I-10125, Turin, Italy
[e] Laser-Laboratorium Göttingen e.V., Hans-Adolf-Krebs-Weg 1, D-37077, Göttingen, Germany
[f] Fraunhofer Institute for Microstructure of Materials and Systems IMWS, Walter-Hülse-Str. 1, D-06120, Halle (Saale), Germany

ARTICLE INFO

Article history:
Received 28 July 2017
Received in revised form
11 October 2017
Accepted 9 November 2017
Available online 11 November 2017

Keywords:
Nanostructured materials
Laser processing
Surface plasmon resonance
Optical spectroscopy
XRD
EXAFS

ABSTRACT

To develop a technique for the production of submicron line patterns and directed arrays of plasmonic nanoparticles, the generation and implantation of gold nanoparticles into float glass surfaces was studied by means of ArF-excimer laser irradiation (193 nm) below the ablation threshold of the glass which was sputter coated with a gold layer with a thickness of 70 nm. The formation of gold particles was confirmed by the characteristic surface plasmon resonance (SPR) peak at ~550 nm. The intensity of the SPR peak of gold particles embedded in the glass matrix increases with the number of applied laser pulses, indicating a different degree of implantation of the gold nanoparticles into the glass surface. It was revealed that the laser implantation of the generated gold particles into the glass is supported on the tin-bath side by the enhanced absorption of tin ions. The dependences of SPR parameters upon the number of laser pulses at different fluences were obtained. Using the methods of X-ray diffraction and extended X-ray absorption fine structure, the mean size of implanted gold particles was estimated at 15–20 nm. This particle size was confirmed by analytical (scanning) transmission electron microscopy, but a small fraction of single particles with a size of ~50 nm have also been observed. The particles arrangement was further examined by the fitting of experimental optical extinction spectra, varying the particles sizes and interparticle distances within the direct calculations of spectra by the multi-spheres T-matrix method, considering the possible agglomerations of particles. The applied experimental technique provides the creation of arrays of gold nanoparticles in the near-surface region of the glass, which can be used as the substrates or nuclei in the glass for producing bimetallic nanoparticles with gold as the core and SPR characteristics varied in a wide range of visual wavelengths.

1. Introduction

In recent years, gold and silver nanoparticles in glasses or on glass surfaces have been intensively studied because of their unique optical properties [1–5]. The presence of the surface plasmon resonance (SPR) in their optical extinction spectra [6–9] enables the localization of the electromagnetic field within nanometer distances [10]. It was established that SPR characteristics in monometallic gold or silver nanoparticles depend upon their sizes and therefore can be tuned by producing particles of the required size [11–13]. Different experimental techniques for the production of gold and silver nanoparticles in glass were suggested including a melt-quenching technique [14] in which gold particles are formed during the glass fabrication and the doping of a glass matrix with gold ions and additional thermal heating [15]. Mäder et al. generated arrays of gold nanodots on silicon substrates [16]. However, to construct suitable devices for applications in nanoplasmonics [17] or optical data transfer such as nano-antennas or nano-gratings,

* Corresponding author.
E-mail address: bugaev@sfedu.ru (L.A. Bugaev).

https://doi.org/10.1016/j.jallcom.2017.11.122
0925-8388/

directed arrays of plasmonic nanoparticles that are incorporated into the glass matrix have to be generated. This implies that it is necessary to develop methods for nanoparticles incorporation within the glass matrix and generation of submicron line patterns and directed arrays of plasmonic gold or silver nanoparticles in the near-surface region of the glass. Tatchev et al. [18] and Sheng et al. [19] studied the formation of arrays of gold nanoparticles by means of X-ray irradiation of gold doped soda-lime silicate glass. However, the reported size of the generated gold particles in that study did not exceed 4 nm and therefore the position of the SPR peak cannot be tuned. The space-selective growth of plasmonic silver and gold nanoparticles can also be obtained by means of UV excimer laser irradiation below the ablation threshold of the glass (without damaging the glass surface) using the corresponding masks [20,21]. Henley et al. [22,23] generated abrasion-resistant arrays of gold nanoparticles by means of the KrF-excimer laser irradiation (248 nm) of glass surfaces, which had been coated with a thin gold layer with a thickness of between 4 and 10 nm. In a first step, UV laser irradiation caused the disintegration of the gold layer, by which gold nanoparticles are formed. In a second step, the nanoparticles are incorporated into the glass surface due to further UV laser irradiation. This process is referred to as the laser implantation of nanoparticles, which is extensively developing [22–25]. The performed studies of optical extinction spectra of the generated monometallic silver and gold nanoparticles in glass show that, depending upon the particles' size and degree of agglomeration, the shape of SPR is changed and its wavelength position can be shifted within ~50 nm.

A promising approach for creating submicron line patterns and directed arrays of plasmonic nanoparticles with a SPR position tuned in a wide range of wavelengths is the synthesis of bimetallic gold/silver alloy nanoparticles [26] or nanoparticles with core-shell architecture [27] through the UV ArF-excimer laser irradiation (193 nm) below the ablation threshold of the glass, varying the number of pulses at different fluences. A theoretical study [27] of the dependence of the SPR in such bimetallic core-shell nanoparticles upon their different size and architecture shows that the wavelength position of the SPR can be shifted from ~410 to 620 nm. In order to propose a reliable experimental technique for the synthesis of directed arrays of such bimetallic core-shell nanoparticles with gold as a core and silver as a shell, a clear understanding of the formation of the gold nanoparticles under the laser pulses as possible substrates or nuclei for the precipitation of the silver atoms is required. Therefore, in this work we present the study of the formation of gold nanoparticles in soda-lime silicate float glass by means of the ArF-excimer laser irradiation of the glass that has been sputter coated with a gold layer with a thickness of 70 nm. Special attention is paid to the study of the processes, which occur as a result of the interaction of the laser light with the gold layer – the necessary first step to produce gold particles of controlled sizes – which in turn is the precondition to create core-shell particles of a gold core and a silver shell with defined SPR characteristics. In preliminary tests, we performed the experiments by using gold layers with a thickness of 35 nm and 70 nm and found that the concentration of generated gold particles is much higher by using a gold layer with a thickness of 70 nm. The tin-bath side of the float glass (Fig. 1a illustrates the used notations for the sides of the glass) exhibits an increased absorption at the wavelength of approximately 200 nm due to the existence of Sn^{2+} and Sn^{4+} ions [28], which is close to the used laser wavelength (193 nm). In this regard, the laser irradiation of the gold-coated air side and the gold-coated tin-bath side of the float glass and its effect on the generation and implantation of gold nanoparticles has been studied in a first step (Sec. 3.1). Furthermore, the implantation of the gold nanoparticles as a result of irradiating the gold-coated tin-bath side has been

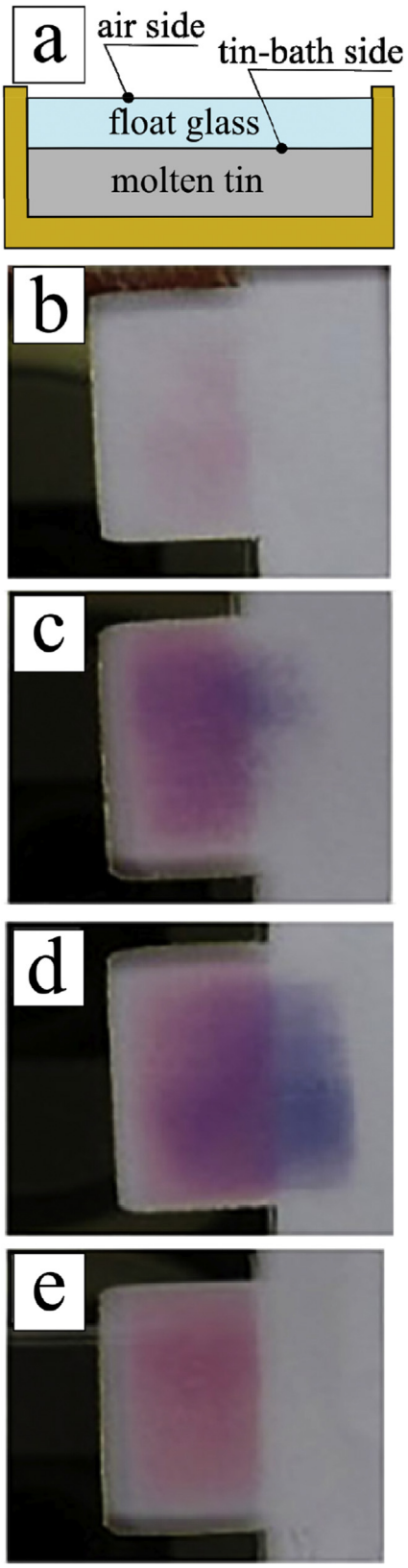

Fig. 1. Used notations for the sides of the glass sample – (a) and pictures of the samples after gold coating and subsequent laser irradiation by 10 laser pulses at the tin-bath side (b–d) and at the air side (e) of the float glass. The fluence of the first laser pulse was 120 mJ/cm^2 (b), 130 mJ/cm^2 (c) and 140 mJ/cm^2 (d and e). The average laser fluence in all cases was 140 mJ/cm^2. On the right side of the laser spots non-implanted gold particles have been removed by wiping with a dry cloth.

investigated by scanning electron microscopy (Sec. 3.2). The interaction of the first laser pulse with the gold layer and its influence on the size and concentration of nanoparticles has been analyzed by optical spectroscopy (Sec. 3.3). Finally, the size and arrangement of implanted gold nanoparticles have been determined by analytical (scanning) transmission electron microscopy including energy-dispersive X-ray spectroscopy (Sec. 3.4), extended X-ray absorption fine structure (Sec. 3.5) and X-ray diffraction (Sec. 3.6). In addition, the fitting of optical extinction spectra was performed by applying the multi-scattering T-matrix approach (Sec. 3.7), which enables the taking into consideration of possible particle agglomerations.

2. Experimental methods

In this work we used soda-lime silicate float glass (thickness 1 mm) of the following composition of the tin-bath side (weight-%): 75,4% SiO_2, 4,2% Na_2O, 7,1% B_2O_3, 4,3% MgO, 8,2% CaO, 0,7% Al_2O_3, 0,3% K_2O, 0,02% SnO_2. The composition of the air side is the same except for SnO_2. The glass samples have been cleaned with acetone and then sputter coated with gold (thickness 70 nm) either at the tin-bath side or at the air side of the float glass (Sputtercoater EMITECH K550; current: 20 mA, Ar pressure: 10^{-1} mbar). As a next step, ArF-excimer laser irradiation (Lambda Physik LPX 315; wavelength: 193 nm, pulse duration: 20 ns) has been applied to the gold-coated side of the glass. Because of pulse-to-pulse fluctuations we had to consider the average laser fluence, which was 140 mJ/cm^2 for all sample irradiations, whereas the fluence of each laser pulse was measured simultaneously using a beam splitter. The repetition rate was 1 Hz and the size of the laser spots was in the rage of 6 × 6 mm^2 to 10 × 10 mm^2.

Preliminary X-ray diffraction measurements were performed at BM01b (now moved to BM31) beamline of European Synchrotron Radiation Facility (ESRF) and indicated the presence of weak peaks on the positions close to that of *fcc* Au. However, the strong diffuse scattering of the glass led to low signal to background ratio of the patterns measured in Debye-Scherrer geometry. To evidence the presence of the nanoparticles, XRD measurements were repeated in Bragg-Brentano geometry for both laser irradiated tin-bath side of the soda-lime glass and its rear (not gold-coated) side were measured using a Bruker D2 PHASER diffractometer with Cu K_α source ($\lambda = 1.5418$ Å). The X-ray tube was operated at 30 kV and 10 mA. The data collection was performed in the 2θ range from 20° to 70° with 0.05° step in 2θ and acquisition time 10 s per point. In order to obtain a better signal to noise ratio for crystalline size determination, the Au (111) reflection was measured separately using a position-sensitive LynxEye detector fixed centered at 2θ ~ 38.3° covering the 2θ range from 35.5° to 41.2°. The samples were cleaned with acetone prior to diffraction measurements, so that the XRD signal should originate from the implanted gold particles.

Au L_3-edge extended X-ray absorption fine structure (EXAFS) spectra were measured at the μ-Spot beamline of the BESSY-II Synchrotron Radiation Facilities (Berlin, Germany) [29]. All spectra were measured at room temperature in fluorescence yield mode. The photon energy scanning steps were adjusted to $\delta E = 1.0$ eV and $\delta k = 0.05$ Å^{-1} in the XANES and EXAFS regions respectively, where E is the energy of the incident radiation and k is the photoelectron wavenumber.

Analytical (scanning) transmission electron microscopy ((S)TEM) measurements including energy-dispersive X-ray spectroscopy (EDX) were performed using a FEI Titan3 80-300 electron microscope using an acceleration voltage of 200 kV. STEM images were obtained using a high-angle annular dark field detector (HAADF, Fischione Model 3000). EDX was performed using a Super-X EDX detector equipped with four SDD detectors (FEI company). The STEM sample preparation was done by a purely mechanical wedge-polishing routine (polishing system MultiprepTM, Allied company), followed by a low-energy (2.5 keV) Ar^+ broad beam final milling step (precision ion polishing system PIPS, Gatan company) to achieve electron transparency and to remove any residues from the mechanical polishing. To provide electric conductivity during the (S)TEM investigations the samples have been coated with a thin carbon layer.

By means of TEM, XRD and EXAFS measurements we investigated only those gold particles, which have been implanted into the glass, i.e. gold particles embedded in the glass matrix. Non-implanted gold particles are located on the glass surface and can be removed by cleaning with acetone or by wiping with a dry cloth. Consequently, to investigate the progressive implantation of the gold nanoparticles by scanning electron microscopy (SEM) using a Zeiss EVO MA 10, the surfaces of the respective samples were not cleaned after the laser irradiation to retain all generated gold particles. For SEM investigations, the samples have been additionally sputter coated with a thin metallic film (thickness 10 nm) to provide electric conductivity. It was observed, that the metallic film does not influence the gold nanoparticles. The SEM investigations were performed at an accelerating voltage of 20 kV.

Optical extinction spectra have been measured by an UV/Vis/NIR spectrometer (Perkin Elmer, Lambda 900) in the wavelength range from 300 nm to 800 nm. To reduce the spot size to the laser irradiated areas a circular aperture with a diameter of 3 mm has been used.

3. Results and discussion

3.1. Influence of the air side and the tin-bath side as well as of the fluence of the first laser pulse

Results of applying 10 laser pulses to the gold-coated glass samples are shown in Fig. 1(b–e). Fig. 1d and (e) as well as Fig. 2a and (b) were already presented in Ref. [30]. Due to the pulse-to-pulse fluctuations of the laser we have to consider the average laser fluence, which was 140 mJ/cm^2 for all sample irradiations. In all cases a red coloration can be observed on the left side of the laser spots in Fig. 1, which is caused by the SPR of non-implanted gold nanoparticles located on the glass surface. However, as can be seen from Fig. 1b–d, the result of the laser irradiation of the gold-coated tin-bath side strongly correlates with the fluence of the first laser pulse, which was 120 (b), 130 (c) and 140 mJ/cm^2 (d). Especially the amount of implanted gold nanoparticles increases with the fluence of the first laser pulse, as can be seen on the right side of the laser spots, where the non-implanted gold particles have been removed by wiping with a cloth. In some cases (Fig. 1c and d) a blue coloration can be observed, which is caused by the gold nanoparticles implanted in the glass matrix. The change of the color from red to blue is possibly caused by the change of the refraction index of the surrounding medium of the gold particles during the implantation of the latter into the glass or by an increase of the size of the gold particles. Fig. 1e illustrates the result of irradiating of the gold-coated air side of the float glass under the same conditions referring to Fig. 1d, that means the same average laser fluence and the same fluence of the first laser pulse, which was 140 mJ/cm^2. As can be seen from Fig. 1e, no gold particles have been implanted into the glass. Thus, the result of the laser irradiation depends among others on the substrate (here tin-bath side and air side of the float glass) and on the fluence of the first laser pulse, noting that in all cases the average laser fluence was 140 mJ/cm^2. Especially, the amount of implanted gold particles increases with the fluence of the first laser pulse.

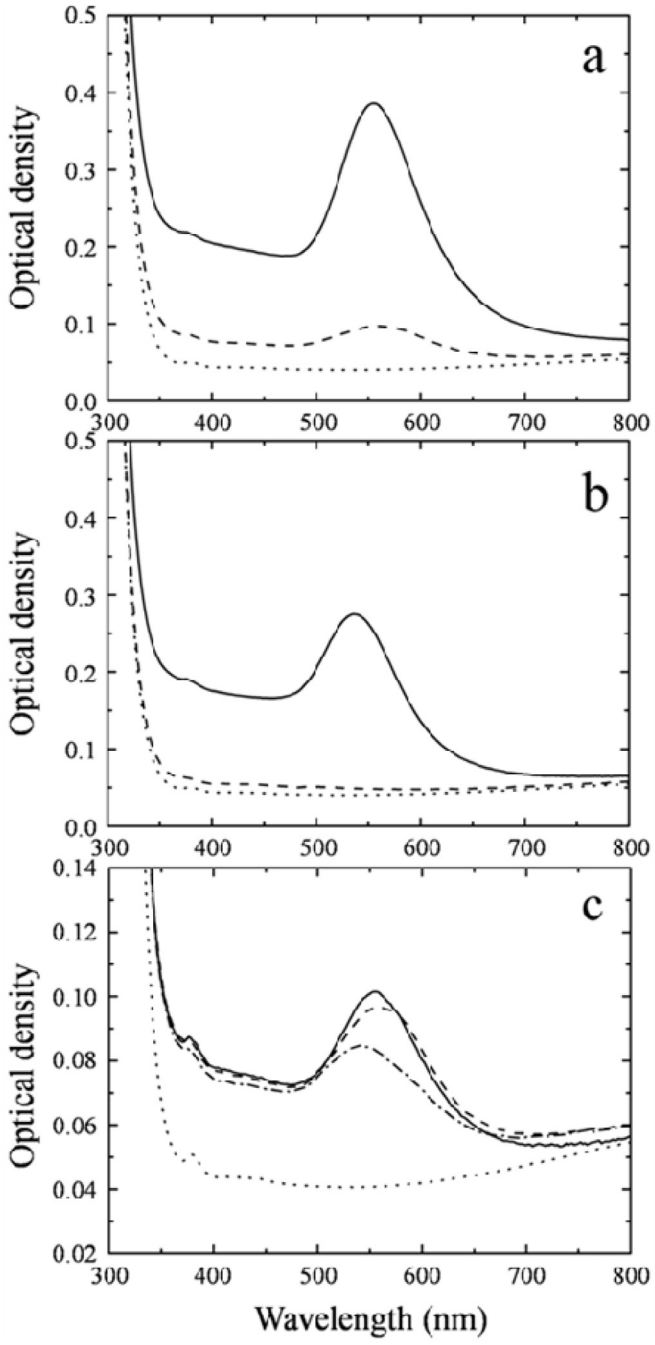

Fig. 2. (a and b): Changes in optical extinction spectra as a result of irradiating the gold-coated tin-bath side (a) and the air side (b) by 10 laser pulses (fluence of the first laser pulse as well as average laser fluence was 140 mJ/cm^2) before cleaning (solid curve) and after cleaning (dashed curve) of the laser irradiated areas with acetone. (c): Optical extinction spectra as a result of irradiating the gold-coated tin-bath side by 5 (dashed dotted curve), 10 (dashed curve) and 50 (solid curve) laser pulses (fluence of the first laser pulse was 140 mJ/cm^2 in all cases) and subsequent cleaning of the laser irradiated areas with acetone. Dotted curve in (a), (b) and (c) corresponds to basic glass.

The position of the SPR peak at approximately 540–550 nm as shown in Fig. 2a, b and c confirms the formation of gold particles by laser irradiation of the gold layer. By irradiating the gold-coated air side, the generated gold particles have been removed completely after cleaning with acetone, as can be seen by the disappearance of the SPR peak in Fig. 2b (dashed curve) in contrast to Fig. 2a. We suppose that this effect can be explained by the increased absorption coefficient of the glass at the tin-bath side at the wavelength of 200 nm due to tin ions [28], which implicates a much higher temperature rise of the glass surface above the glass transformation temperature by each laser pulse. This results in a much lower viscosity as compared to the air side, which in turn promotes the implantation of the gold particles into the glass matrix. For this reason, further results, which will be discussed in this paper, refer to the laser irradiation of the gold-coated tin-bath side. Fig. 2c illustrates that the amount of implanted gold particles increases with the number of laser pulses. The effect of the number of applied laser pulses on the particles size distribution is investigated in Section 3.7 by means of the fitting of these optical spectra. The implantation process of the gold particles will be investigated by SEM images in the next section.

3.2. SEM investigations of the implantation process

SEM images in Fig. 3 illustrate the formation and implantation of gold particles by irradiating the gold-coated tin-bath side of the float glass. Here, the samples are tilted by 80°. Fig. 3a illustrates the surface of the gold layer before the laser irradiation. The surface of the tin-bath side of the basic glass without gold coating is comparable to Fig. 3a (not shown). As can be seen from Fig. 3c, spherical particles of size of approximately 50 nm have been generated by the second laser pulse. These particles are located on the glass surface. Particles of size smaller than 20 nm that will be shown in Fig. 8 cannot be resolved in these images. By applying further laser pulses (50 laser pulses in Fig. 3d), the particles have been immersed into the glass due to the melting of the glass surface by each single laser pulse. However, there is no cumulative heating. That means that the glass surface has been cooled down to room temperature already before the next laser pulse arrives. As can be seen from Fig. 3b, no gold particles have been generated yet after one laser pulse, however the appearance of heterogeneities in the arrangement of Au atoms in the film is observed. Gold nanoparticles (Fig. 3c) are formed during the second laser pulse. Further laser pulses lead to the implantation of the gold nanoparticles into the glass surface (Fig. 3d). The interaction of the first laser pulse with the sputtered gold layer, the formation of gold nanoparticles during the second laser pulse and their implantation into the glass by the following pulses will be discussed and clarified in the next section.

3.3. Interactions with the gold layer by the first and further laser pulses

After applying only one laser pulse to the gold-coated tin-bath side of the float glass, a grey coloration of the laser irradiated area can be observed at fluences greater than 120 mJ/cm^2, while total transparency occurs at lower fluences down to a threshold fluence at approximately 50 mJ/cm^2, below which the gold layer remains unaffected. This threshold fluence depends on the thickness of the gold film and on the thermal properties of the substrate [31]. Between 50 and 120 mJ/cm^2 there are no visible residuals of gold on the glass, which indicates ablation of the gold film. Fig. 4 shows two laser spots, which have been generated by a single laser pulse at fluences of 100 mJ/cm^2 and 140 mJ/cm^2, respectively.

By means of optical extinction spectra (Fig. 5) it could be verified that the grey coloration is caused by a thin residual gold layer, whose formation can be explained either by the deposition of gold on the glass surface after total ablation of the gold layer or by partial ablation of the gold layer, where a thin gold layer remains. By increasing the laser fluence from 120 mJ/cm^2 onwards, the coloration changes from pale grey to dark grey. Regarding the optical spectra shown in Fig. 5, it can be seen that the thickness of the

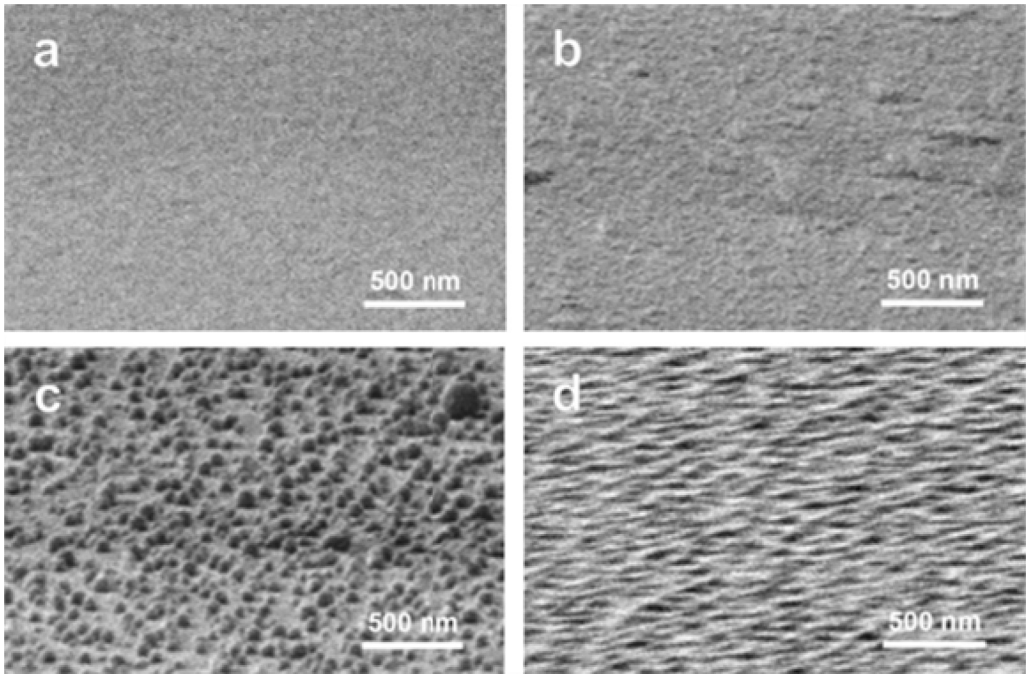

Fig. 3. SEM images (tilt angle 80°) of the surface of gold-coated float glass at the tin-bath side without laser irradiation (a) and after one laser pulse (b), two laser pulses (c) and 50 laser pulses (d). The average laser fluence as well as the fluence of the first laser pulse was 140 mJ/cm^2. The surface of the samples was not cleaned after laser irradiation.

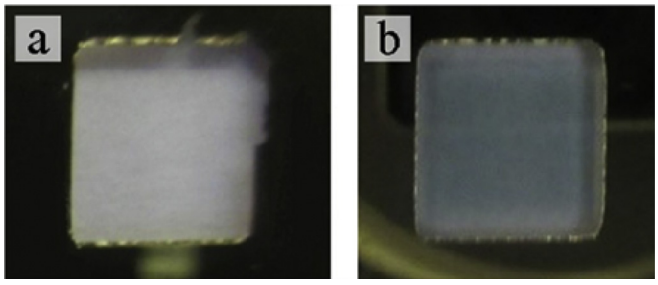

Fig. 4. Laser spots generated by single laser pulses at 100 mJ/cm^2 (a) and 140 mJ/cm^2 (b) at the gold-coated tin-bath side of the float glass without cleaning after laser irradiation.

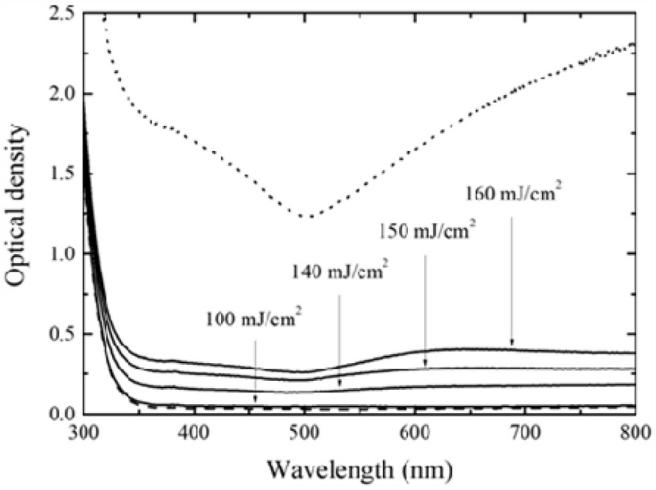

Fig. 5. Optical extinction spectra as a result of a single laser pulse applied to the gold-coated tin-bath side of the float glass at fluences of 100 mJ/cm^2, 140 mJ/cm^2, 150 mJ/cm^2 and 160 mJ/cm^2 (solid curves). The dotted curve corresponds to a non-irradiated gold layer (thickness 70 nm), the dashed curve corresponds to the basic glass. The laser irradiated areas were not cleaned.

residual gold layer increases by increasing the laser fluence from 140 to 160 mJ/cm^2, while at a fluence of 100 mJ/cm^2, the spectrum is similar to that of the basic glass. This can be explained as follows: during the laser irradiation, the formation of an ablation plume near to the glass surface takes place, due to melting and vaporization of the gold layer and the glass surface. On the one hand, a part of the incident laser energy can be absorbed by this plume. On the other hand, the re-deposition of ablated or vaporized gold on the glass surface can be enhanced by the plasma pressure developing with increasing fluence in the plume [32,33].

According to the optical extinction spectra, the thicknesses of the residual gold layers have been determined by subtracting the basic glass and regarding the spectrum of the non-irradiated gold layer (thickness 70 nm) as a reference. The values are listed in Table 1.

Table 1
Thicknesses of the residual gold layers after a single laser pulse, as determined by the extinction spectra (Fig. 5) after basic glass subtraction.

Fluence of the single laser pulse	Thickness of the residual gold layer
140 mJ/cm^2	6 nm
150 mJ/cm^2	11 nm
160 mJ/cm^2	14 nm

If further laser pulses are applied to the areas that have already been influenced by the single laser pulse, the grey color turns into red already by the first laser pulse of this second irradiation, which indicates the formation of gold particles, as observed in the SEM images in Fig. 3. While a considerable amount of the sputtered gold layer is ablated by the first laser pulse, the residual gold layer melts during the second pulse [23,31]. This leads to the formation of gold droplets due to perforation and Rayleigh instability of the molten gold film [23]. A small amount of gold will also be vaporized. These

two different processes (ablation by the first laser pulse and melting by the second one) can be attributed to the different film thicknesses, which were 70 nm for the initial (sputtered) gold layer and 6 to 14 nm for the residual gold layer. The formation of the gold droplets or particles after the second laser pulse (see Fig. 3c), accompanied by the appearance of discontinuities and a thinning of the gold film as a result of the first laser pulse, causes a decrease of the amount of laser energy, which is absorbed by the gold because of its fragmentation, which results in the reduction of the laser radiation absorption cross-section in comparison to the continuous gold film. This leads in turn to the increased absorption by the glass surface, which is enhanced at the tin-bath side of the glass due to the presence of tin ions. Thus, the laser irradiation of the tin-bath side of the glass leads to the decrease of the viscosity of the glass surface due to melting and as a consequence, the implantation of the gold particles into the glass by the third and further laser pulses is provided.

Optical extinction spectra as a result of a total of five laser pulses are shown in Fig. 6, noting that the samples were not cleaned in this case - all generated gold particles, especially non-implanted particles, have been retained. It can be seen that the fluence of the first laser pulse, which determined the thickness of the residual gold layer, influences the position of the SPR peak due to different particle sizes (especially size distributions) as well as the area below the curves due to different volume fractions of the gold particles. It is obvious, that the volume fraction of the generated gold particles increases with the fluence of the first laser pulse due to the increasing thickness of the residual gold layer. These results demonstrate that the laser irradiation of a gold layer of thickness 70 nm enables to tune the SPR peak by varying the fluence of the first laser pulse.

3.4. Results of (S)TEM investigations

The arrangement and the size of the gold particles were investigated by means of TEM (Fig. 7a) and STEM (Fig. 7b). Here we consider only implanted gold particles, because non-implanted particles were removed during the sample preparation.

Both images (Fig. 7a and b) show the cross section of the glass surface as a result of irradiating the gold-coated tin-bath side by 10 laser pulses (fluence of the first laser pulse: 140 mJ/cm^2). It can be seen that the gold particles are located directly below the glass surface, which was slightly affected in Fig. 7b during the TEM sample preparation. The diameter of the smaller particles is approximately 15 nm and that of the larger ones is approximately 50 nm, which is also confirmed in Fig. 7c by the EDX Au-L$_\alpha$ linescans across the smaller particles (linescan 1) and across a larger one

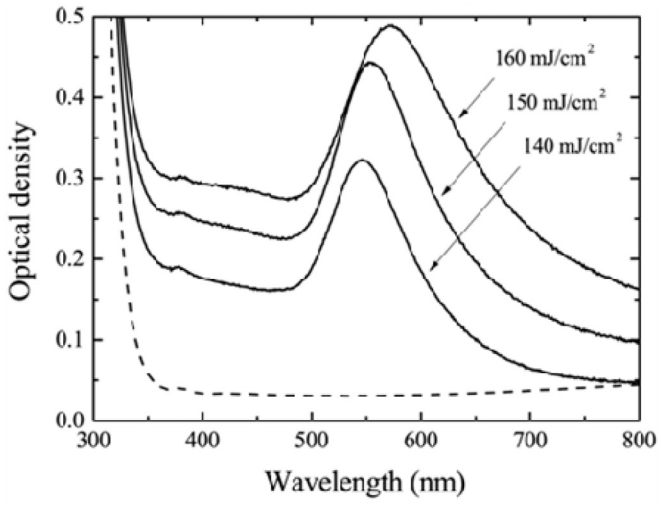

Fig. 6. Changes in the optical extinction spectra as a result of irradiating the gold-coated tin-bath side by 5 laser pulses at an average laser fluence of 140 mJ/cm^2, whereas the fluence of the first laser pulse was 140 mJ/cm^2, 150 mJ/cm^2 and 160 mJ/cm^2 as denoted. Dashed curve corresponds to the basic glass. The laser irradiated areas were not cleaned.

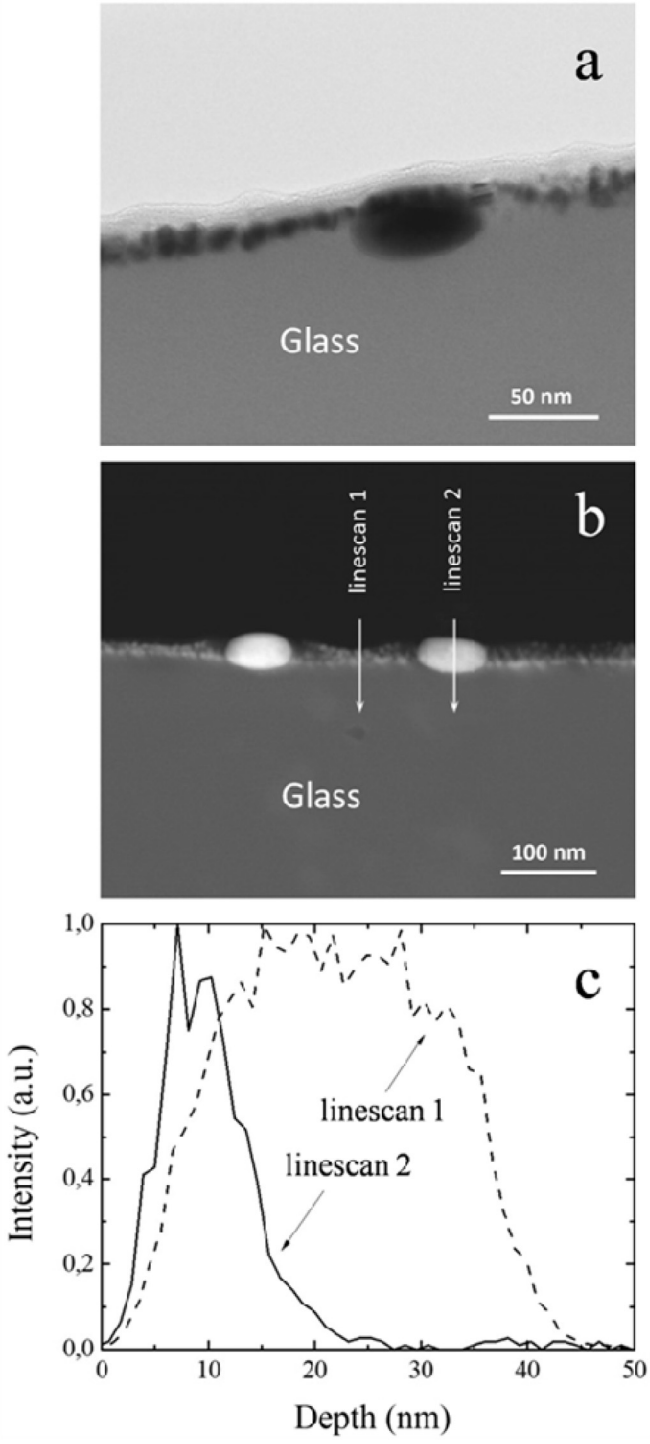

Fig. 7. TEM (a) and STEM (b) image as a result of irradiating the gold-coated tin-bath side by 10 laser pulses (fluence of the first laser pulse: 140 mJ/cm^2). (b) denotes the positions of performed EDX Au-L$_\alpha$ linescans, which can be seen in (c). The depth 0 corresponds to the glass surface.

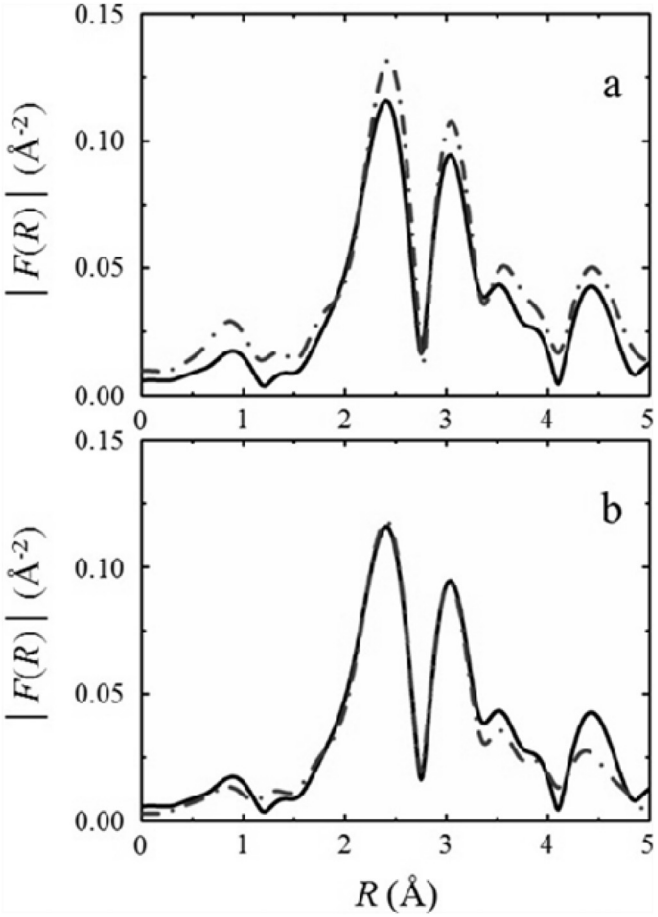

Fig. 8. FT magnitudes $|F(R)|$ of $k\,\chi(k)$, obtained by Δk interval with $k_{min} = 2.15$ Å^{-1} and $k_{max} = 10.1$ Å^{-1}: (a) – for experimental Au L_3-edge EXAFS in the gold foil (dashed curve) and in the sample irradiated by 50 laser pulses (solid curve); (b) – for experimental Au L_3-edge EXAFS in the same sample (solid curve) and for the best fit model based on eq. (1) (dashed curve).

(linescan 2).

3.5. Results of Au L_3-EXAFS analysis

The structural characterization of the gold nanoparticles formed in the glass was performed also by Au L_3-edge EXAFS. The oscillatory parts $\chi(k)$ of experimental Au L_3-edge EXAFS spectra (k – photoelectrons wave number) in samples after irradiation by 5 and 10 laser pulses are similar in the shape and position of features to those of the sample irradiated by 50 pulses. This can be explained by the fact that the nanoparticles are formed already after the second laser pulse. Further irradiation leads to changes in their sizes and better implantation of the gold nanoparticles into the glass. The non-implanted gold particles were removed from the surface by cleaning with acetone when the laser irradiation was finished. As a result, the sample exposed to 50 laser pulses contains larger amount of implanted gold particles which leads both in EXAFS and in XRD to the better signal to noise ratio. For this reason, only sample exposed to 50 laser pulses was chosen for the analysis.

The experimental spectra were processed using the technique for diminishing the effect of correlations among the fitting parameters on their obtaining values [34,35]. The used approach enables to determine the percentage (C) of atoms located in the internal (usually structurally ordered) region of a mean monometallic nanoparticle from the total number of atoms in the nanoparticle and gives average values of parameters, characterizing the structure of its near-surface region.

In the studied glass samples, the experimental EXAFS signal is averaged over the different structural states of gold atoms (different types of the local structure) in each sample. The simplest structural model of a nanoparticle which can be used to account for such differences should contain two structural states of the absorbing metal atom [34,35]: Au(1) – atoms in the internal or core region of the nanoparticle and Au(2) – atoms of the near surface or shell region, that usually contains lattice distortions and defects. The applicability of this model for the studied glass sample is provided by Fig. 8a, which compares the magnitudes of the Fourier transforms $|F(R)|$ of the Au L_3-edge EXAFS spectra in the gold foil reference and in the glass sample irradiated by 50 laser pulses. The comparison shows that in the extended R-range (up to ~ 5 Å), all the peaks in $|F(R)|$ of the gold foil reference are present in the $|F(R)|$ of the sample, but with reduced magnitudes. This indicates the presence of an *fcc* like structure for at least the part of the gold atoms, which are located in the ordered core region of the gold nanoparticles. Such atoms are denoted in the following as Au(1) and according to [34] the fit model for EXAFS oscillatory part $\chi(k)$ was used based on the expression:

$$\chi_{model}(k) = C\chi_{Au(1)}(k) + (1 - C)\chi_{Au(2)}(k) \quad (1)$$

where C is the percentage of Au(1) atoms and $\chi_{Au(2)}(k)$ is the contribution of gold atoms attributed to the near-surface region of the nanoparticle and denoted as Au(2). To reduce the number of variables and correlations among them, providing the stability of the obtained values of parameters, the term $\chi_{Au(1)}(k)$ in (1) was constructed according to [34] as $\chi_{Au(1)}(k) = \chi^{experim}_{Au-foil}(k)*\exp(-2*\Delta\sigma^2_{Au(1)}k^2)$. In this expression, the function $\chi^{experim}_{Au-foil}(k)$ was obtained from experimental Au L_3-edge EXAFS in the gold foil and hence, contained the exact contribution from the first and more distant shells of the Au(1) atoms. The factor $\exp(-2*\Delta\sigma^2_{Au(1)}k^2)$ takes into account the difference in structural order in the first shell of a gold atom in a nanoparticle with that of one in the foil. For the gold foil, $\Delta\sigma^2_{Au(1)} = 0$ by definition, and the obtaining of noticeable values of $\Delta\sigma^2_{Au(1)}$(>0.001 Å^2) will indicate that the *fcc* structure is either distorted or the fit doesn't require the function $\chi^{experim}_{Au-foil}(k)$, and our assumption on an *fcc* internal region in the gold nanoparticles would hence be wrong. The reduction factor $S^2_0(Au - Au)$ was fixed to its value in the gold foil: 0.89 for both Au(1) and Au(2) atoms. In this approach, backscattering amplitudes and phase shifts are not needed for the construction of the term $\chi_{Au(1)}(k)$ in (1) for the fit and hence, the adjustable energy parameter $e_0(Au(1))$ was not used. As a result, only two variable parameters were used for the first term in (1) in the fit of $F(R)$: global parameter C and $\Delta\sigma^2_{Au(1)}$. For the term $\chi_{Au(2)}(k)$ in (1), the "single-path" approximation was used according to [34] to account for the contribution of the particle's near-surface region. The fit model for the gold local structure based on (1) reproduces all the features of the $F(R)$ of experimental Au L_3-edge EXAFS in the sample in the extended R-range (Fig. 8b), giving the following values of parameters: $\Delta\sigma^2_{Au(1)} = 0.0003$ Å^2 and $C = 68\%$.

The mean size (D) of gold particles can be estimated then using this value of C and the dependence $C(D)$ of [35] obtained for palladium nanoparticles on the two different dielectric supports (Al_2O_3, SiO_2) by combination of TEM and EXAFS results. The "size equation" $C(D)$ contains only two adjustable parameters A, β which

depend upon the character of particle's surface (density of atoms in the near-surface or "shell" region, defects in it) and particles shape. The presence of the similar internal regions with *fcc* like structure in both palladium and gold nanoparticles provided by EXAFS, and the identity of the shapes for the main amount of gold nanoparticles of sizes <30 nm with the palladium ones provided by TEM images, enabled to estimate the mean size D of gold nanoparticles using the dependence $C(D)$ of [35]. By this approach, the value of D in the sample irradiated by 50 laser pulses can be estimated as D ~11 nm. However, taking into account an error in the determination of the parameters A, β [35] and the non-linearity of the equation for $C(D)$, the size evaluation produces the values varied from 9 to 19 nm, so that the final estimation of D is 14 ± 5 nm, which is in agreement with the size of the main amount of the smaller particles in the TEM image (Fig. 7a). One more possible source of errors (~0.4 nm) in the estimation of the particles size can be due to the difference in the cell parameters of palladium and gold, which is however, on the order less than the fitting error of ~ ± 5 nm. The modeling of the mean gold nanoparticle by the spherical cluster with the revealed *fcc* structure of the core and the percentage $C = 68\%$ of Au(1) atoms attributed to this core, confirmed the obtained value of the particle size D ~ 15 nm and gave an estimate for the thickness of the disordered shell (near-surface region of gold nanoparticle) consisting of Au(2) atoms as ~ 1 nm.

3.6. Results of XRD measurements

The intensity of X-ray scattering by different components, coexisting in the sample, is proportional to the relative fractions of these components within the area irradiated by the incoming X-ray beam. Due to this fact, the scattering from the gold nanoparticles is overshadowed by the intense background from the amorphous glass. Therefore, to extract the signal corresponding to the gold particles, we collected XRD patterns for both laser irradiated tin-bath side and for the rear side of the glass, which contains no gold particles. The XRD measurements were performed for glass samples after their surfaces had been cleaned with acetone, which removed the non-implanted particles from the surface of the glass. In this case, the difference in XRD patterns from the irradiated side and rear side of the sample can be attributed to the scattering of the gold nanoparticles implanted in the subsurface layer of the irradiated side.

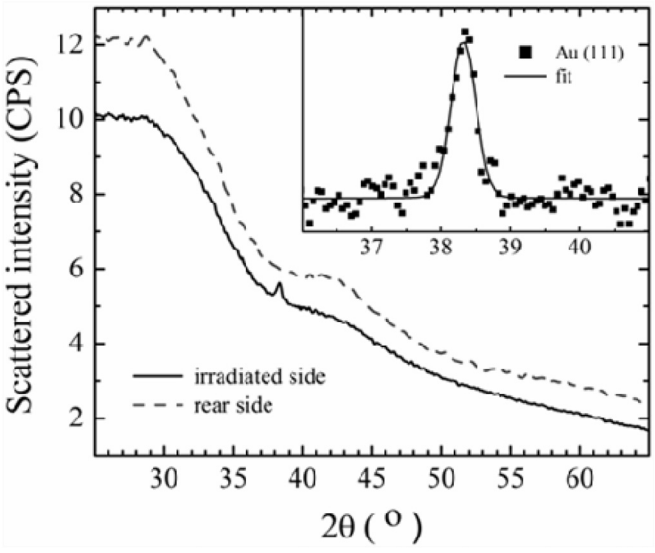

Fig. 9. XRD pattern of implanted gold particles (solid curve) as a result of irradiating the gold-coated tin-bath side by 50 laser pulses (fluence of the first laser pulse: 140 mJ/cm^2) and subsequent cleaning by acetone. The dashed pattern corresponds to the scattering from the rear side of the float glass also after cleaning by acetone. Both patterns for laser irradiated side and rear side are shown without normalization, background subtraction and vertical shift. The inset shows the background subtracted experimental Au (111) reflection fitted by a Pseudo-Voight function.

Fig. 9 presents the XRD patterns of both sides of the sample, which was irradiated at the gold-coated tin-bath side by 50 laser pulses (fluence of the first laser pulse: 140 mJ/cm^2). XRD patterns of samples after irradiation by 5 and 10 laser pulses have the same features at 2θ ~38°, but with lower signal to noise ratio, so only the sample exposed to 50 laser pulses was chosen for the analysis. The clearly observed feature at 2θ ~38° for the irradiated side of the sample corresponds to the Au (111) reflection, which evidences the presence of implanted gold particles with *fcc* structure of their internal region in agreement with the EXAFS result. However, it must be noted that also a small amount of non-implanted gold particles could be detected since it is difficult to remove all gold particles from the glass surface. The Au(111) reflection was fitted by a Pseudo-Voight function, whose full width at half maximum (FWHM) provided a mean gold particle size of $D = 20 \pm 5$ nm according to the Debye-Scherrer equation [36]. The calculated lattice parameter according to the Au (111) peak position was determined as $a = 4.07 \pm 0.01$ Å. However, the actual error in determining the absolute value of a is higher, since the Bragg peak position is affected by the cell parameter and the instrumental shift of the zero angle, which was not considered, because its correlation with the cell parameter cannot be resolved by refining of only one peak.

3.7. Fitting of optical extinction spectra by applying the T-matrix approach

The sizes of gold nanoparticles, estimated by XRD, TEM and EXAFS methods in Sec. 3.4 - 3.6, were verified and refined by using their values as input for the fit of the optical extinction spectra of implanted gold particles, obtained as a result of irradiating the gold-coated tin-bath side by 5, 10 and 50 laser pulses (fluence of the first laser pulse: 140 mJ/cm^2) and subsequent cleaning of the glass surface with acetone. The optical extinction of nanoparticles was extracted from the experimental spectrum by subtracting the basic glass optical density from the observed optical density. The obtained residual optical density was fitted by a theoretical spectrum which was calculated using the multi-spheres T-matrix method code (MSTM) [37] with additional scale multiplication and background addition. The T-matrix approach allows to simulate the electromagnetic wave scattering and absorption on agglomerates of spherical particles. The wavelength-dependent dielectric constant of gold was set to experimental values from the Johnson-Christy database [38]. The calculated spectrum was averaged over all orientations of a given nanoparticle agglomerate, which was performed in a numerically effective way within a T-matrix approach. The variation of particle positions and sizes was performed using a developed python script [39], based on heavily rewritten code for dimer simulations in space dust by D. Mayerich [40]. The fitting to the experimental signals was performed using the BFGS [41–43] method as it is implemented in the scientific python (SciPy) library [44,45]. In addition, the cases of overlapped spheres were detected and skipped, so that the optimization routine can be freely continued without producing non-physical results, where the T-matrix approach would not be applicable.

Fig. 10a–c shows the results of the fit, which was performed using spherical gold particles with equal initial size of each particle of 15 nm, placed on an ideal cubic mesh with interparticle distances of 20 nm as an input. These initial values were chosen according to XRD and EXAFS results, and TEM-based size information for the

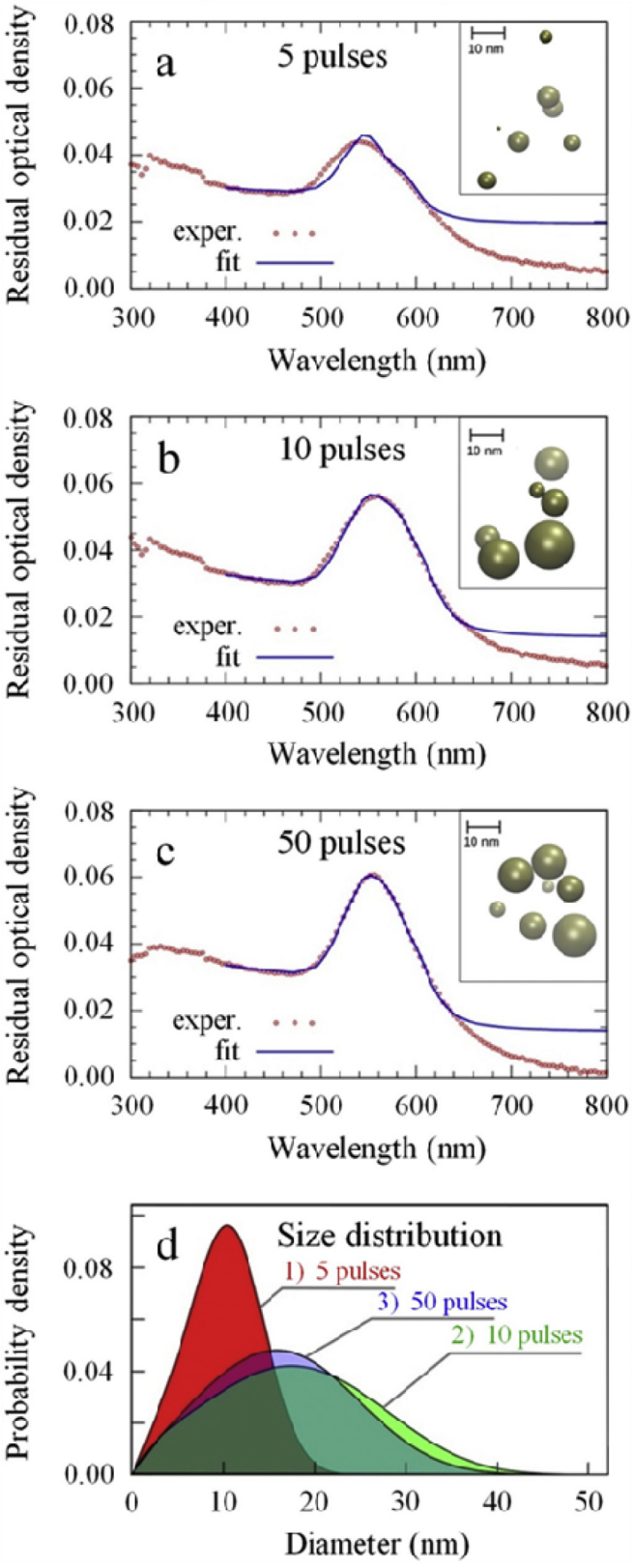

Fig. 10. Parts (a–c): comparison of experimental (red circles) and fitted (blue solid lines) optical extinction spectra of the samples with the gold-coated tin-bath side irradiated by 5 (a), 10 (b) and 50 (c) laser pulses, which correspond to Fig. 2c. The insets illustrate the corresponding arrangements of gold particles provided by the fit. Part (d) illustrates the size distribution of particles obtained by the fitting. (For interpretation of the references to colour in this figure legend, the reader is referred to the web version of this article.)

prevailing amount of gold nanoparticles in the sample (the effect of the presence of a few particles with sizes of ~50 nm in the sample treated by 50 pulses is considered below). According to Fig. 10d, as a result of 5 laser pulses, the size of implanted gold particles is approximately 10 nm and increases to approximately 20 nm by applying 10 and 50 laser pulses. The fit of the spheres radii and positions resulted in agglomerates with different structures shown in the insets of Fig. 10a–c. Some disagreements of the fitting curve with the experimental spectrum for the sample after 5 pulses on Fig. 10a can be probably caused by the presence of a noticeable amount of very small nanoparticles with sizes less than 10 nm, whose dielectric function differs from that for the bulk gold used in our approach (so called 'internal' size effect). The size of ~10 nm is considered as a boundary size, which delimits 'external' and 'internal' size effects [46,47] originated from particle geometry changes and dielectric constant changes, respectively. Indeed, in the case of the sample irradiated by 5 pulses, the experimental position of the SPR peak at 540 nm already indicates the presence of particles smaller than 10 nm, since the SPR peak of an isolated gold particle with size of ~10 nm should be located at ~550 nm according to both T-matrix and Mie-theory simulations. The size estimation for such small particles from optical spectra is complicated due to the unknown dielectric function, but in spite of the poor fit quality in Fig. 10a, the sizes of the particles obtained by the fitting procedure are reasonably smaller than for other considered samples, so that the results for the sample treated by 5 pulses seem to be qualitatively correct.

For other two samples, the fit quality allows to determine the parameters of particles sizes and agglomerates which are in agreement with the results of other used experimental techniques. The particle size distributions shown in Fig. 10d were calculated using the non-parametric method of kernel density estimation (KDE) [48] as it is implemented in the programming language and software environment for statistical computing "R" [49] with dynamically chosen kernel width according to the Sheather-Jones prescription [50]. The corresponding values of particle sizes and interparticle distances, averaged over all particles in agglomerates are listed in Table 2. The distribution of sizes for the sample treated by 5 pulses is shifted towards smaller particle sizes, and the distributions for the samples treated by 10 and 50 pulses correspond to larger particles with higher dispersion over sizes. The changes between size distributions for samples after 10 and 50 pulses are minor but they may indicate the destruction of some of the big particles under laser irradiation.

TEM and STEM images of the sample irradiated by 10 laser pulses show that besides of the main amount of gold nanoparticles with smaller sizes, there are a few gold nanoparticles with sizes of ~50 nm, which are absent in the obtained cluster agglomerates (Fig. 10). To elucidate the effect of the presence of these large particles on the SPR peak position, we performed calculations of optical extinction spectra by the MSTM method taking into account the interaction of the multiplicity of smaller particles (of mean size ~ 15 nm) with only one large particle of size 50 nm. The used approximation seems reasonable because TEM results (Fig. 7) shows: i) a few number of large gold nanoparticles and ii) rather different areas of localization of smaller and large gold nanoparticles in the near-surface glass region, caused by the difference in their penetration depth in glass. The comparison of the optical extinction spectra calculated by the model which considers only smaller gold nanoparticles and by the model which accounts the interactions of these smaller gold nanoparticles with the large one is presented in Fig. 11. For the spectrum of the last model, the variation of the particles parameters with the aim to fit it to the experimental spectrum was not performed, which is the reason of differences in peak intensities for the two compared models. This

Table 2
Parameters of the fit of optical extinction spectra presented in Fig. 10.

Number of laser pulses used for irradiation of samples	Average particle diameter, nm	Average interparticle distance, nm
5	9 ± 2	50 ± 20
10	15 ± 5	40 ± 12
50	15 ± 3	30 ± 8

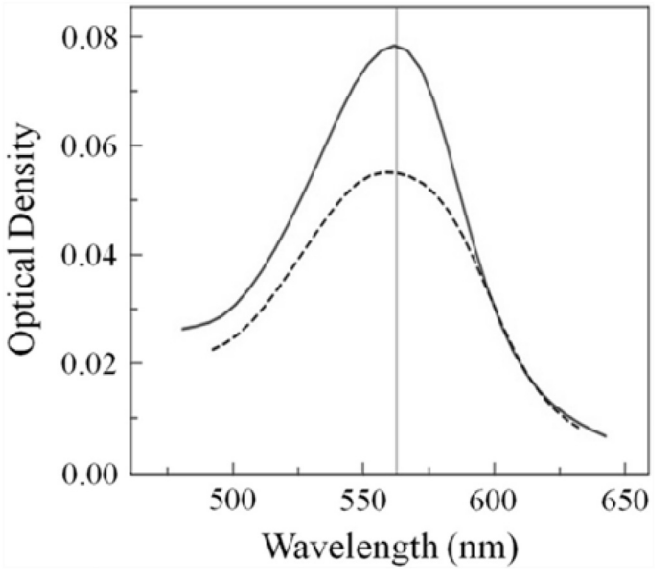

Fig. 11. Optical extinction spectra calculated by the model which accounts the interactions of smaller gold nanoparticles of mean size 15 nm with the large particle of size 50 nm (solid curve) and by the model which considers only smaller gold nanoparticles (dashed curve).

comparison shows that the interaction of the gold nanoparticles of mean size ~15 nm with the large gold nanoparticles of size 50 nm doesn't change the position of the SPR peak formed by these smaller particles.

4. Conclusions

The performed study of the generation and implantation of gold nanoparticles into float glass surfaces by means of ArF-excimer laser irradiation (193 nm) below the ablation threshold of the glass, which was sputter coated with a gold layer with a thickness of 70 nm, allows to make the following conclusions:

- by applying only one laser pulse to the gold-coated float glass, a threshold fluence at approximately 120 mJ/cm^2 was revealed, below which the total ablation of the gold layer occurs. At fluences greater than 120 mJ/cm^2, a residual gold layer is formed, whose thickness increases with the fluence of the laser pulse. By applying one further laser pulse, the residual gold layer melts and gold droplets (particles) are formed due to layer perforation and the Rayleigh instability of the molten gold film. The concentration of generated gold particles increases with the thickness of the residual gold layer, which is determined by the fluence of the first laser pulse. These particles are located on the surface of the glass and can be easily removed by cleaning with acetone or wiping with a dry cloth. By applying further laser pulses at an average laser fluence of 140 mJ/cm^2, the implantation of these particles into the surface of the glass takes place at the tin-bath side of the float glass. Here, the glass surface melts due to the increased absorption at approximately 200 nm due to tin ions, which leads to the immersion of the gold particles into the molten glass. By irradiating the air side, generated gold particles were not implanted by further laser pulses. It was therefore revealed that the laser implantation of the generated gold particles into the glass is supported by the enhanced absorption of the tin ions and hence, the substrate is one of the most important parameters besides the laser wavelength and fluence;
- the intensity of the SPR peak increases with the number of applied laser pulses, indicating a different degree of implantation of the gold nanoparticles into the glass surface. The dependences of SPR parameters upon the number of laser pulses at different fluences were obtained;
- the structural characterization of the gold nanoparticles implanted in the tin-bath side of the glass by 50 laser pulses at an average laser fluence of 140 mJ/cm^2 was performed by two complementary methods of XRD and EXAFS. Both methods gave the distinct evidence of the presence of gold nanoparticles with an *fcc* core structure. The mean size of the particles obtained by the processing of XRD patterns (20 ± 5 nm) is slightly larger than that obtained from EXAFS (14 ± 5 nm), however, both values are in reasonable agreement with the TEM data for the sample irradiated by 10 laser pulses: the main amount of gold nanoparticles with sizes of ~15 nm and a very few ones with sizes of ~50 nm.
- the fitting of the experimental optical extinction spectra of the glass samples irradiated by 5, 10 and 50 pulses was performed varying the gold particles' sizes and interparticle distances within the direct calculations of the spectra by the Multi-Spheres T-matrix method, considering possible particle agglomerations. By this approach, it was revealed that the mean particle size increases from 9 to 15 nm with the increasing number of pulses from 5 to 10 and remains stable up to 50 pulses, while the average interparticle distance decreases monotonically. It is also revealed that the presence of a few gold nanoparticles with a size of ~50 nm in the glass sample does not significantly affect the position of the SPR peak formed by a multitude of smaller particles with a mean size of ~15 nm.

The applied experimental technique provides the creation of arrays of gold nanoparticles in the near-surface region of glass, which can be used as substrates or nuclei in the glass for producing bimetallic nanoparticles with gold as the core and SPR characteristics, varied in a wide range of visual wavelengths.

Acknowledgements

M.H., M.D. would like to thank DFG-project № DU 214/14-1 for financial support. V.V.S., L.A.A., A.V.S., V.V.P. and L.A.B. acknowledge the grant of Southern Federal University (ВнГр-07/2017-06). Authors are thankful to Dr. I. Zizak for the help during XAFS measurements at the micro-Spot beamstation of the Synchrotron Radiation Facility BESSY II (Berlin, Germany).

References

[1] S. Eustis, M.A. El-Sayed, Why gold nanoparticles are more precious than pretty gold: noble metal surface plasmon resonance and its enhancement of the radiative and nonradiative properties of nanocrystals of different shapes, Chem. Soc. Rev. 35 (2006) 209–217, https://doi.org/10.1039/b514191e.
[2] O.A. Yeshchenko, I.M. Dmitruk, A.A. Alexeenko, M.Y. Losytskyy, A.V. Kotko, A.O. Pinchuk, Size-dependent surface-plasmon-enhanced photoluminescence from silver nanoparticles embedded in silica, Phys. Rev. B 79 (2009) 235438, https://doi.org/10.1103/PhysRevB.79.235438.
[3] M.A. Garcia, Surface plasmons in metallic nanoparticles: fundamentals and applications, J. Phys. D Appl. Phys. 44 (2011) 283001, https://doi.org/10.1088/

0022-3727/45/38/389501.
[4] O.A. Yeshchenko, I.S. Bondarchuk, V.S. Gurin, I.M. Dmitruk, A.V. Kotko, Temperature dependence of the surface plasmon resonance in gold nanoparticles, Surf. Sci. 608 (2013) 275–281, https://doi.org/10.1016/j.susc.2012.10.019.
[5] E.S. Sazali, M.R. Sahar, S.K. Ghoshal, R. Arifin, M.S. Rohani, A. Awang, Optical properties of gold nanoparticle embedded Er^{3+} doped lead-tellurite glasses, J. Alloys Compd. 607 (2014) 85–90, https://doi.org/10.1016/j.jallcom.2014.03.175.
[6] R. Philip, G.R. Kumar, Picosecond optical nonlinearity in monolayer-protected gold, silver, and gold-silver alloy nanoclusters, Phys. Rev. B 62 (2000) 13160–13166, https://doi.org/10.1103/PhysRevB.62.13160.
[7] S. Qu, Y. Gao, X. Jiang, H. Zeng, Y. Song, J. Qiu, C. Zhu, K. Hirao, Nonlinear absorption and optical limiting in gold-precipitated glasses induced by a femtosecond laser, Opt. Commun. 224 (2003) 321–327, https://doi.org/10.1016/S0030-4018(03)01761-9.
[8] J. Wilcoxon, Optical absorption properties of dispersed gold and silver alloy nanoparticles, J. Phys. Chem. B 113 (2009) 2647–2656, https://doi.org/10.1021/jp806930t.
[9] S.K. Ghosh, T. Pal, Interparticle coupling effect on the surface plasmon resonance of gold nanoparticles: from theory to applications, Chem. Rev. 107 (2007) 4797–4862, https://doi.org/10.1021/cr0680282.
[10] E. Hao, G.C. Schatz, Electromagnetic fields around silver nanoparticles and dimers, J. Chem. Phys. 120 (2004) 357–366, https://doi.org/10.1063/1.1629280.
[11] W. Haiss, N.T.K. Thanh, J. Aveyard, D.G. Fernig, Determination of size and concentration of gold nanoparticles from UV-Vis Spectra, Anal. Chem. 79 (2007) 4215–4221, https://doi.org/10.1021/ac0702084.
[12] K.L. Kelly, E. Coronado, L.L. Zhao, G.C. Schatz, The optical properties of metal nanoparticles: the influence of size, shape, and dielectric environment, J. Phys. Chem. B 107 (2003) 668–677, https://doi.org/10.1021/jp026731y.
[13] S. Link, M.A. El-Sayed, Size and Temperature Dependence of the plasmon absorption of colloidal gold nanoparticles, J. Phys. Chem. B 103 (1999) 4212–4217, https://doi.org/10.1021/jp984796o.
[14] R. Rajaramakrishna, C. Saiyasombat, R.V. Anavekar, H. Jain, Structure and nonlinear optical studies of Au nanoparticles embedded in lead lanthanum borate glass, J. Non Cryst. Solids 406 (2014) 107–110, https://doi.org/10.1016/j.jnoncrysol.2014.09.052.
[15] J. Vosburgh, R.H. Doremus, Optical absorption spectra of gold nano-clusters in potassium borosilicate glass, J. Non Cryst. Solids 349 (2004) 309–314, https://doi.org/10.1016/j.jnoncrysol.2004.08.211.
[16] M. Mäder, S. Perlt, T. Höche, H. Hilmer, M. Grundmann, B. Rauschenbach, Gold nanostructure matrices by diffraction mask-projection laser ablation: extension to previously inaccessible substrates, Nanotechnol 21 (2010) 175304, https://doi.org/10.1088/0957-4484/21/17/175304.
[17] M.I. Stockman, Nanoplasmonics: past, present, and glimpse into future, Opt. Express 19 (2011) 22029–22106, https://doi.org/10.1364/OE.19.022029.
[18] D. Tatchev, A. Hoell, M. Eichelbaum, K. Rademann, X-ray-assisted formation of gold nanoparticles in soda lime silicate glass: suppressed ostwald ripening, Phys. Rev. Lett. 106 (2011), 085702, https://doi.org/10.1103/PhysRevLett.106.085702.
[19] J. Sheng, K. Kadono, T. Yazawa, Nanosized gold clusters formation in selected areas of soda-lime silicate glass, J. Non Cryst. Solids 324 (2003) 295–299, https://doi.org/10.1016/S0022-3093(03)00320-X.
[20] M. Dubiel, M. Heinz, M. Stiebing, J. Meinertz, J. Ihlemann, T. Rainer, Generation and characterization of plasmonic nanostructures in glass surfaces by means of excimer and solid state laser irradiation, Proc. SPIE 9163 (2014), https://doi.org/10.1117/12.2061034, 91631M.
[21] M. Heinz, V.V. Srabionyan, A.L. Bugaev, V.V. Pryadchenko, E.V. Ishenko, L.A. Avakyan, Y.V. Zubavichus, J. Ihlemann, J. Meinertz, E. Pippel, M. Dubiel, L.A. Bugaev, Formation of silver nanoparticles in silicate glass using excimer laser radiation: structural characterization by HRTEM, XRD, EXAFS and optical absorption spectra, J. Alloys Compd. 681 (2016) 307–315, https://doi.org/10.1016/j.jallcom.2016.04.214.
[22] S.J. Henley, M.J. Beliatis, V. Stolojan, S.R.P. Silva, Laser implantation of plasmonic nanostructures into glass, Nanoscale 5 (2013) 1054–1059, https://doi.org/10.1039/C2NR33629D.
[23] S.J. Henley, J.D. Carey, S.R.P. Silva, Pulsed-laser-induced nanoscale island formation in thin metal-on-oxide films, Phys. Rev. B 72 (2005), https://doi.org/10.1103/PhysRevB.72.195408, 195408.
[24] C. Sánchez-Akéa, A. Canales-Ramosa, T. García-Fernándezb, M. Villagrán-Muniza, Nanosecond pulsed laser nanostructuring of Au thin films: comparison between irradiation at low and atmospheric pressure, Appl. Surf. Sci. 403 (2017) 448–454, https://doi.org/10.1016/j.apsusc.2017.01.181.
[25] K. Grochowska, G. Śliwiński, A. Iwulska, M. Sawczak, N. Nedyalkov, P. Atanasov, G. Obara, M. Obara, Engineering Au nanoparticle arrays on SiO2 glass by pulsed UV laser irradiation, Plasmonics 8 (2013) 105–113, https://doi.org/10.1007/s11468-012-9428-3.
[26] N. Kumar, F. Alam, V. Dutta, Deposition of Ag and Au-Ag alloy nanoparticle films by spray pyrolysis technique with tuned plasmonic properties, J. Alloys Compd. 585 (2014) 312–317, https://doi.org/10.1016/j.jallcom.2013.09.145.
[27] C. Zhang, B. Chen, Z. Li, Surface plasmon resonance in bimetallic core-shell nanoparticles, J. Phys. Chem. C 119 (2015) 16836–16845, https://doi.org/10.1021/acs.jpcc.5b04232.
[28] D. Ehrt, Review - phosphate and fluoride phosphate optical glasses - properties, structure and applications, Phys. Chem. Glas. Eur. J. Glass Sci. Technol. Part B 56 (2015) 217–234, https://doi.org/10.13036/17533562.56.6.217.
[29] Helmholtz-Zentrum Berlin für Materialien und Energie, The mySpot beamline at BESSY II, J. Large Scale Res. Facil. 2 (2016), https://doi.org/10.17815/jlsrf-2-113. A102.
[30] M. Heinz, M. Dubiel, J. Meinertz, J. Ihlemann, A. Hoell, Investigation of gold and bimetallic gold/silver nanoparticles in soda-lime-silicate glasses formed by means of excimer laser irradiation, Proc. SPIE 10093 (2017), https://doi.org/10.1117/12.2249751, 100930I.
[31] E. Matthias, M. Reichling, J. Siegel, O.W. Käding, S. Petzoldt, H. Skurk, P. Bizenberger, E. Neske, The influence of thermal diffusion on laser ablation of metal films, Appl. Phys. A 58 (1994) 129–136, https://doi.org/10.1007/BF00332169.
[32] M. von Allmen, A. Blatter, Laser-beam Interactions with Materials - Physical Principles and Applications, Springer, Berlin, Heidelberg, New York, 1995, https://doi.org/10.1007/978-3-642-57813-7.
[33] D. Hülsenberg, A. Harnisch, A. Bismarck, Microstructuring of Glasses, Springer, Berlin, Heidelberg, New York, 2008.
[34] V.V. Srabionyan, A.L. Bugaev, V.V. Pryadchenko, A.V. Makhiboroda, E.B. Rusakova, L.A. Avakyan, R. Schneider, M. Dubiel, L.A. Bugaev, EXAFS study of changes in atomic structure of silver nanoparticles in soda-lime glass caused by annealing, J. Non Cryst. Solids 382 (2013) 24–31, https://doi.org/10.1016/j.jnoncrysol.2013.09.025.
[35] V.V. Srabionyan, A.L. Bugaev, V.V. Pryadchenko, L.A. Avakyan, J.A. van Bokhoven, L.A. Bugaev, EXAFS study of size dependence of atomic structure in palladium nanoparticles, J. Phys. Chem. Solids 75 (2014) 470–476, https://doi.org/10.1016/j.jpcs.2013.12.012.
[36] A.L. Patterson, The Scherrer formula for X-ray particle size determination, Phys. Rev. 56 (1939) 978–982, https://doi.org/10.1103/PhysRev.56.978.
[37] D. Mackowski, M. Mishchenko, A multiple sphere t-matrix Fortran code for use on parallel computer clusters, J. Quant. Spectrosc. Radiat. Transf. 112 (2011) 2182–2192, https://doi.org/10.1016/j.jqsrt.2011.02.019.
[38] P.B. Johnson, R.W. Christy, Optical constants of the noble metals, Phys. Rev. B 6 (1972) 4370–4379, https://doi.org/10.1103/PhysRevB.6.4370.
[39] G. van Rossum, Python tutorial. Technical Report CS-R9526, Centrum voor Wiskunde en Informatica (CWI), Amsterdam, 1995.
[40] D. Mayerich, A GUI Interface for the Multiple-sphere T Matrix (MSTM) Package, 2015. https://git.stim.ee.uh.edu/optics/mstm-gui. (Accessed 26 April 2017).
[41] C.G. Broyden, The convergence of single-rank quasi-Newton methods, Math. Comp. 24 (1970) 365–382, https://doi.org/10.1090/S0025-5718-1970-0279993-0.
[42] D. Goldfarb, A family of variable-metric methods derived by variational means, Math. Comp. 24 (1970) 23–26, https://doi.org/10.1090/S0025-5718-1970-0258249-6.
[43] D.F. Shanno, P.C. Kettler, Optimal conditioning of quasi-Newton methods, Math. Comp. 24 (1970) 657–664, https://doi.org/10.1090/S0025-5718-1970-0274030-6.
[44] T.E. Oliphant, Python for scientific computing, Comput. Sci. Eng. 9 (2007) 10–20. http://www.scipy.org. (Accessed 7 June 2017).
[45] K.J. Millman, M. Aivazis, Python for scientists and engineers, Comput. Sci. Eng. 13 (2011) 9–12, https://doi.org/10.1109/MCSE.2011.36.
[46] N.G. Khlebtsov, V.A. Bogatyrev, L.A. Dykman, A.G. Melnikov, Spectral extinction of colloidal gold and its biospecific conjugates, J. Colloid Interface Sci. 180 (1996) 436–445, https://doi.org/10.1006/jcis.1996.0323.
[47] X. Fan, W. Zheng, D.J. Singh, Light scattering and surface plasmons on small spherical particles, Light Sci. Appl. 3 (2014), https://doi.org/10.1038/lsa.2014.60 e179.
[48] W.N. Venables, B.D. Ripley, Modern Applied Statistics with S, Springer, New York, 2002, p. 495.
[49] R. Core Team, R: a Language and Environment for Statistical Computing, R Foundation for Statistical Computing [Online], 2014. http://www.R-project.org/. (Accessed 26 April 2017).
[50] S.J. Sheather, M.C. Jones, A reliable data-based bandwidth selection method for kernel density estimation, J. R. Stat. Soc. B 53 (1991) 683–690.